Plasmonic Nanocrystal Solar Cells Utilizing Strongly Confined Radiation

Natalia Kholmicheva,[†,§,#] Pavel Moroz,[†,§,#] Upendra Rijal,[§,||] Ebin Bastola,[§,⊥] Prakash Uprety,[§,⊥] Geethika Liyanage,[§,⊥] Anton Razgoniaev,[†,‡] Alexis D. Ostrowski,[†,‡] and Mikhail Zamkov*[,†,§]

[†]The Center for Photochemical Sciences, [‡]Department of Chemistry, and [§]Department of Physics, Bowling Green State University, Bowling Green, Ohio 43403, United States, [⊥]Department of Physics, University of Toledo, Toledo, Ohio 43606, United States, and [||]Department of Physics, Wayne State University, Detroit, Michigan 48202, United States. [#]N.K. and P.M. contributed equally to this work.

ABSTRACT The ability of metal nanoparticles to concentrate light *via* the plasmon resonance represents a unique opportunity for funneling the solar energy in photovoltaic devices. The absorption enhancement in plasmonic solar cells is predicted to be particularly prominent when the size of metal features falls below 20 nm, causing the strong confinement of radiation modes. Unfortunately, the ultrashort lifetime of such near-field radiation makes harvesting

the plasmon energy in small-diameter nanoparticles a challenging task. Here, we develop plasmonic solar cells that harness the near-field emission of 5 nm Au nanoparticles by transferring the plasmon energy to band gap transitions of PbS semiconductor nanocrystals. The interfaces of Au and PbS domains were designed to support a rapid energy transfer at rates that outpace the thermal dephasing of plasmon modes. We demonstrate that central to the device operation is the inorganic passivation of Au nanoparticles with a wide gap semiconductor, which reduces carrier scattering and simultaneously improves the stability of heat-prone plasmonic films. The contribution of the Au near-field emission toward the charge carrier generation was manifested through the observation of an enhanced short circuit current and improved power conversion efficiency of mixed (Au, PbS) solar cells, as measured relative to PbS-only devices.
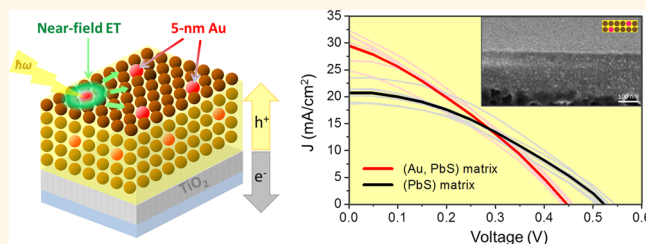
KEYWORDS: lead sulfide · plasmonics · colloidal quantum dots · inorganic matrix · near field

The spatial confinement of light near metal surfaces gives rise to remarkable optical properties that are highly attractive for the development of light-harvesting materials. Of a particular interest are nanoparticles of noble metals, where the per-volume extinction coefficient in the visible range exceeds those of semiconductor quantum dots or organic polymers by at least an order of magnitude (see Figure 1a).[1−8] These superior light extinction properties arise from an enhanced density of states associated with the surface plasmon (SP) resonance of free carriers, which funnels incident photons into localized "hot spots". The ability of metal NPs to concentrate light holds strong promise for improving the performance of photovoltaic and photocatalytic materials provided that an efficient strategy for converting the absorbed energy into spatially separated charges is conceived.[9−11]

Recently, the prospect of incorporating plasmonic materials in solar cell devices has received a great deal of attention.[9,12−23] Several strategies for enhancing the cell's optical extinction either through solution-processing or *via* vapor-deposition of plasmonic structures have been considered. Au or Ag metals, exhibiting a strong plasmon resonance in the visible range, have been a common choice of plasmonic materials, although the use of Pt,[24] Pd,[24] Al,[25,26] and Cu[27] has also been explored. Overall, the improvement in the photovoltaic performance of plasmonic devices was attributed to the enhanced optical extinction of an active layer, which allowed decreasing the absorber thickness enabling shorter carrier extraction distances.[28,29] The benefits of the reduced charge collection path, however, were partly compromised by the decrease in the carrier diffusion length caused by the presence of metal dopants in the film.

The confining geometry of metal nanoparticles plays a critical role in the ensuing mechanism of the plasmon energy conversion. Depending on the size of the metal
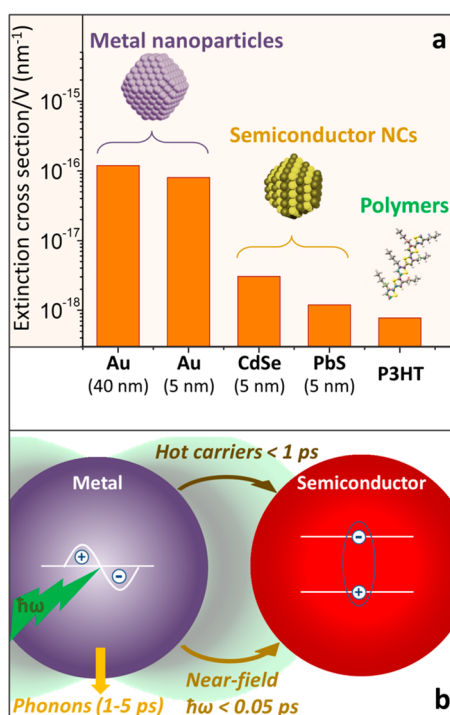
Figure 1. (a) Per-volume extinction cross sections of common nanoscale sensitizers. The comparison highlights superior light-harvesting characteristics of Au nanoparticles relative to semiconductor quantum dots and organic polymers (P3HT).[3−8] **(b)** Schematic representation of the surface plasmon relaxation in small-diameter Au NPs. The decoherence of SP oscillations takes less than 50 fs leading to the generation of hot carriers, which eventually decay by coupling to phonon modes in 1−5 ps.

domain, the operation of plasmonic solar cells can fall into one of the two regimes corresponding to far-field and near-field energy transfer modes. When the size of metal structures is large (>50 nm), most of the absorbed radiation is scattered into the far field, whereby increasing the effective light path in a film. On the contrary, the employment of small-size metal features invokes near-field scattering of radiation, which leads to a subwave confinement of light (Figure S2). The plasmon energy conversion can then undergo *via* a near-field energy or electron transfer.[30]

To date, *far field* scattering of light in plasmonic photovoltaic devices has been a more common choice of the absorption enhancement strategy. An important benefit of this scheme lies in the reduction of the parasitic absorbance through the use of large-size metal features, which couple most of the incident light back into the film (Figure S1). Typically, the location and geometry of plasmonic scatterers can be optimized to form photonic arrays yielding an improved light-harvesting performance. In the absence of the subwave confinement of light, the maximum absorption enhancement, F, for such far-field scattering mode, is given by the Yablonovitch's limit[31] as, $F = 4n^2$ (assuming isotropic emission), where n is the refraction index of the absorber. The actual

enhancement from the far-field scattering is substantially lower since not all of the available momentum states associated with free space modes can be filled.

A recent breakthrough in understanding photonic materials has shown that the classical $4n^2$ limit of absorbance enhancement in photovoltaic films can be surpassed if the radiation modes are confined[32−34] (*e.g.*, using a waveguide structure). It was predicted that for a subwave light confinement with a 5 nm localization length the enhancement of the absorbance can be extended to $F = 60n^2$,[32] up to 15 times greater than in the case of the geometric far-field scattering. Theoretically, such trapping of radiation can be realized through a *near-field* emission of surface plasmons in small-diameter metal nanoparticles where far-field scattering is suppressed (Figure S2). The grand challenge lies in converting the absorbed radiation of small-diameter metal colloids into useful energy, as those structures efficiently couple the electronic decay to phonon modes. Indeed, the decoherence of SP oscillations in metal NPs is extremely fast and takes less than 50 fs[35] leading to the production of hot carriers, which, in turn, decay by coupling to phonon modes in 1−5 ps (see Figure 1b).[36−38] If the plasmon energy or hot carrier population is not transferred away within this short time window, the absorbed radiation will be internalized primarily through the generation of heat. Evidently, such heat production does not contribute to the device photocurrent and is detrimental to the solar cell performance. In order to avoid the thermal dissipation of SP energy, some photovoltaic and photocatalytic schemes have used the energy of hot carriers generated by a dephasing plasmon, which spill over the Schottky barrier and enter the semiconductor phase.[16,17,39−42] This strategy allows collecting some of the plasmon energy before the onset of the thermalization, albeit leading to only a moderate enhancement in the device performance.[42] Nevertheless, the most efficient conversion of the near-field emission is possible when the plasmon energy is picked up *via* the near-field energy transfer prior to its dephasing (Figure 1b). This type of energy exchange can occur through a transfer of virtual photons rather than electrons[43] and was recently shown to enable a record efficiency in polymer solar cells doped with metal nanoparticles.[44]

Here, we demonstrate the development of plasmonic nanocrystal solar cells operating in the near-field energy transfer regime. The gain in the photovoltaic performance is enabled through a resonant coupling of surface plasmon modes in Au nanoparticles to band gap excitations of PbS semiconductor nanocrystals. In order to maximize the confinement of light, the size of Au domains was chosen not to exceed 10 nm in diameter. In this configuration, far field scattering of light is strongly suppressed giving rise to the near-field emission of plasmon radiation. The thermal impact of

residual heating in Au nanoparticles was mitigated through the use of an all-inorganic film design featuring a crystalline matrix encapsulating an array of Au and PbS nanoparticles.[45−47] We show that adding Au NPs into the absorber layer dramatically improves the optical extinction of the film, while causing some curbing of the exciton lifetime due to scattering on Au. The overall benefit of the near-field absorption enhancement strategy was evidenced through a moderate improvement of the solar cell efficiency. For instance, doping the PbS nanocrystal film with 0.3% of Au NPs (by volume) caused an increase in the average power conversion efficiency (PCE) from 4.0 to 4.2%, with the best performing device exhibiting 4.5% of PCE. The increased short circuit current (a gain of $41 \pm 3\%$) was the primary factor contributing to the enhanced PCE, whose effect was partly compromised by a small drop in the open circuit voltage. Possible directions for improving the film morphology toward enhancing the near-field energy conversion are discussed.

RESULTS AND DISCUSSION

Theoretical aspects of photovoltaic absorbers utilizing a strong confinement of optical modes have been discussed in a recent work of Yu et al.[32] In a simplified interpretation of this model, the absorbance enhancement in thin films is inversely proportional to the light-confinement length, d, such that $F \sim M/d$, where M is the number of resonances in the film. Consequently, increasing the density of optical modes in the film through the enhancement of the light localization should lead to the greater enhancement of optical extinction (see Figure S1). Near-field emission of small-diameter metal NPs satisfies these conditions, offering a practical way for achieving a strong localization of light in semiconductor solids. With these considerations in mind, the photovoltaic architecture developed in this work was targeted toward supporting an efficient energy transfer from the surface plasmons of 5−7 nm Au NPs to band gap and impurity excitations of 3.2 nm PbS nanocrystals.

The solar cell morphology comprising small-diameter Au NPs represents a fundamentally interesting case. On one hand, the suppression of far field scattering in these films should enable a near-field emission with typical length scales comparable to the size of a plasmonic nanoparticle. In this arrangement, the confined optical modes can stimulate the production of excitons in semiconductor films leading to an increased device photocurrent. On the other hand, the extraction of the radiative energy from small-diameter metal NPs is more challenging than in the case of large-diameter structures due to a rapid decay of near-field evanescent waves (<50 fs). One of the goals of this work is to evaluate the very expediency of harvesting such near-field radiation through the generation of excitons and excited carriers in a photovoltaic absorber. Because of the fundamental character of this investigation, the conclusions drawn from experiments are built on qualitative comparisons, which allows omitting some of the device optimization steps.

Enabling an efficient energy transfer between semiconductor and metal nanoparticles is the key to avoiding energy losses associated with electron−phonon scattering. This requirement places several stringent criteria on the design of plasmonic films. First, as discussed above, the size of metal NPs should be sufficiently small to minimize the far field scattering (Figure S2). Second, the energy of the plasmon resonance should be somewhat greater than the band gap of the semiconductor absorber in order to promote a fast, one-directional energy transfer while minimizing the phonon generation from above the gap (intraband) vibrational relaxations. Third, to prevent the transfer of photoinduced charges from semiconductor into metal, the two domains should be insulated by a potential barrier. The latter condition becomes particularly important for interfaces of small-size nanoparticles where Schottky barriers may not exist. Finally, since some fraction of SP energy in metal NPs undergoes electron−phonon relaxation, causing heating of the local environment, the plasmonic solar cell needs to have a greater thermal stability than a nonplasmonic equivalent. With these considerations in mind, we have chosen an all-inorganic active layer morphology comprising Au and PbS nanoparticles as energy transfer partners. To this end, both types of nanocrystals were encapsulated into CdS matrices using a previously developed semiconductor matrix encapsulated nanocrystal array (SMENA) approach[45,46] with a minimal Au-PbS spacing, R^{min}_{Au-Pbs} of $\approx$2 nm.

The details of the matrix-encapsulation assembly technique[45] are described in the Methods section. In brief, to fabricate a mixed (Au, PbS) absorber film, both Au and PbS NCs were coated with a shell of the matrix material,[54,56] according to the scheme in Figure 2a. The resulting Au/CdS, and PbS/CdS core/shell NPs were then mixed in octane at predefined ratios (see below) and used as "inks" for processing film layers. The original bulky ligands on the nanoparticle surfaces were exchanged with thermally degradable MPA molecules during each cycle of the layer-by-later (LbL) deposition process. After each three cycles, the film was heated to approximately 140−150 °C to remove MPA ligands and promote crystallographic fusion of neighboring CdS shells. In the final step, additional ZnS material was deposited into the pores of the interfused nanoparticle solid by means of the successive ionic layer adsorption and reaction (SILAR) method.[59] This step was designed to further passivate charged surfaces as well as to enhance the refractive index of the film.[48]
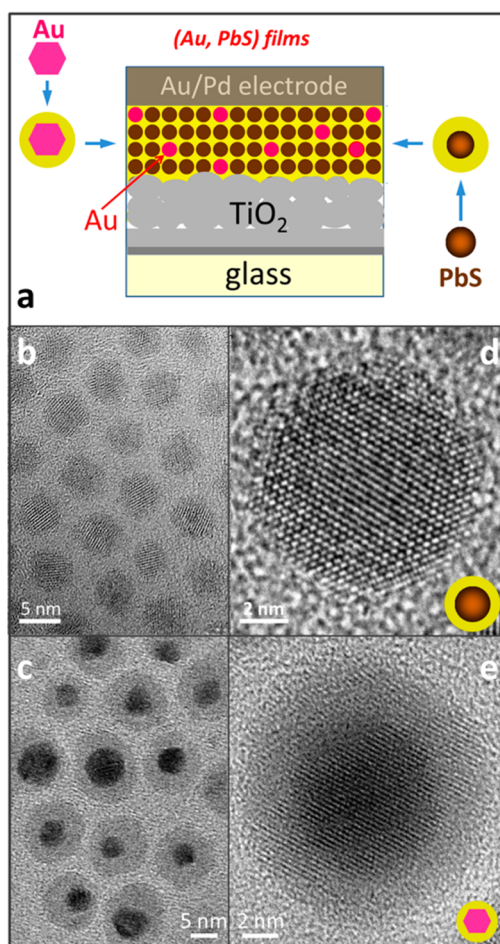
Figure 2. (a) Illustration of the key steps involved in the development of plasmonic solar cells. The colloidal synthesis of PbS/CdS and Au/CdS core/shell NCs is followed by spin-coating of the Au/CdS and PbS/CdS nanocrystal mixture onto TiO₂-modified FTO substrate, the exchange of long-chain ligands with thermally degradable MPA molecules, and crystallographic fusion of core/shell NCs performed using a layer-by-layer deposition. (b, d) Transmission electron microscope (TEM) images of PbS/CdS core/shell NCs used as soluble precursors for the development of the absorber layer. (c, e) TEM images of Au/CdS core/shell NCs.

Figure 2 shows characteristic Transmission Electron Microscope (TEM) images of Au/CdS (c,e) and PbS/CdS (b,d) core/shell nanostructures that served as colloidal precursors for the assembly of photovoltaic films. The growth of the CdS shell onto PbS NCs was carried out using previously established protocols, thorough a $Pb^{2+} \rightarrow Cd^{2+}$ cation exchange.[53] Here, a 0.25 nm CdS shell was employed to provide some degree of quantum confinement for photoinduced carriers in PbS NCs, while enabling interparticle tunneling of charge carriers.[48] In the case of Au NPs, the thickness of the CdS shell was allowed to grow up to 2 nm in order to provide a sufficient potential barrier to both carrier types, whereby shielding PbS electrical charges from the excited states in metal. In this geometry, the rate of carrier tunneling between adjacent PbS domains is expected to be much greater than the rate of PbS to Au charge transfer, thus suppressing carrier scattering on Au domains. The formation of a thick ($\Delta H \approx 2$ nm) CdS shell on Au nanocrystals is evident in a high resolution TEM image of a characteristic Au/CdS core/shell structure (Figure 2e). The uniform placement of the CdS semiconductor around the Au core manifests the absence of an interfacial strain between the two domains, which is a distinct advantage of the cation-exchange growth strategy. As illustrated in Figure S3, the deposition of CdS or ZnS semiconductor shell was accompanied by a red-shift of the plasmon resonance from $\lambda_{Au} \approx 520$ nm to $\lambda_{Au/CdS} = 575$ nm resulting from the changes in the surrounding dielectric constant.

A potential issue concerning the performance of plasmonic solar cells is a trade-off between the enhanced absorbance of a mixed (Au, PbS) nanoparticle film and the reduced photoconductivity of a solid due to carrier scattering on Au domains. If a near-field energy transfer (Au to PbS) is not efficient, the absorber film would require a high concentration of Au NPs in order to reach a sizable "plasmonic" effect. At such high levels of Au doping, however, carrier diffusion length may become too short. This would cause the current density to decrease, compromising an overall benefit of the plasmonic light-harvesting scheme. Along these lines, one of the overarching goals of this work was to understand whether the plasmon-exciton (near-field) energy transfer mechanism is efficient enough to avail the device performance despite adverse effects of metal nanoparticles in the absorber layer.

We first look into the effect of Au doping on the optical density of mixed (Au, PbS) nanocrystal films. Since the per-volume extinction coefficient of Au NPs is about 30 times greater than that of PbS NCs (see Figure 1a), only a small fraction of Au needs to be introduced for a sizable absorption enhancement. To estimate the concentration of Au NPs in the mixed solid, we have quantified the relationship between molar concentrations of both nanoparticle types in precursor solutions and their respective partial number densities. To this end, precursor solutions of mixed (Au, PbS) nanoparticle colloids were deposited onto a TEM grid and analyzed. The ratio of each nanoparticle type (Au/CdS core/shell *versus* PbS/CdS NCs) can be easily obtained by identifying the corresponding populations of each dot in the TEM specimen as shown in Figure 3a and 3b. The ratio of Au to PbS particles on a TEM grid, n_{TEM}, is then converted to a Au volume fraction, v_{Au}, according to the following equation (see Supporting Information for details of calculation):

$$v_{Au} = \frac{4/3\pi R_{Au}^3}{(\sqrt[3]{n_{TEM}}D_{Pbs}+D_{Au})^3} \qquad (1)$$

where D_{PbS} and D_{Au} are the average diameters of PbS/CdS and Au/CdS NCs, respectively, and R_{Au} is the average radius of the Au core domain (without the CdS shell).

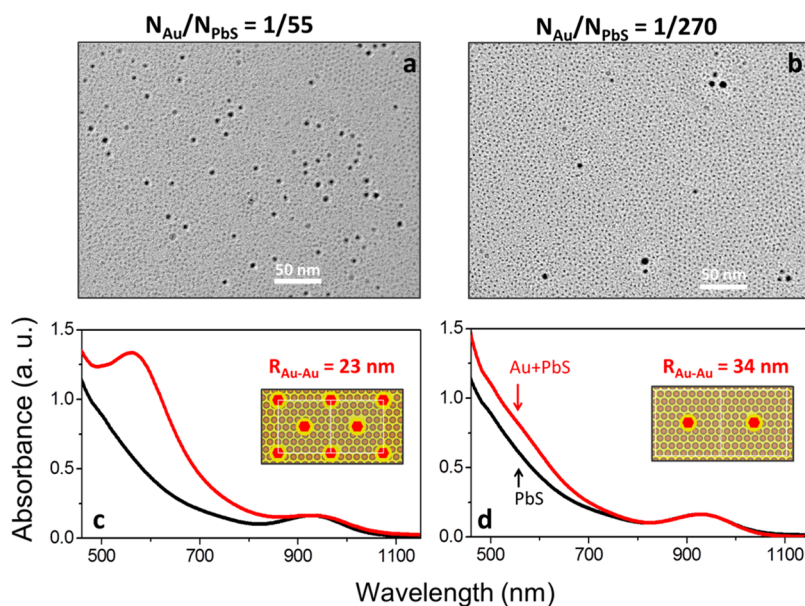$N_{Au}/N_{PbS} = 1/55$ $N_{Au}/N_{PbS} = 1/270$

Figure 3. Illustrating the effect of Au nanoparticles on optical properties of a nanocrystal solid. TEM images of the two nanoparticle mixtures (Au/CdS + PbS/CdS core/shell NCs) corresponding to Au:PbS nanoparticle ratios of 1:55 (a) and 1:270 (b) are shown. The associated solids are expected to have a Au volume fraction of 0.5% (a) and 0.18% (b). The steady-state absorption spectra of mixed nanoparticles samples shown in (a) and (b) are given by a red curve in (c) and (d), respectively. The contribution of the plasmon absorbance is evident through the comparison with PbS/CdS-only samples (black curve).

According to Figures 3 and S4, a noticeable enhancement in the optical extinction of mixed metal—semiconductor films can be achieved with just a small percentage of Au nanoparticles in a solid. For instance, a visible range optical density of a nanoparticle film doubles when the Au volume fraction reaches 0.5%. The TEM images of colloidal "inks" used for film processing are shown in Figures 3a and 3b. The corresponding volume fractions of Au for these samples (v_{Au} = 0.5% (a); v_{Au} = 0.18% (b)) were determined using eq 1. The average Au-to-Au interparticle distance, R_{Au-Au}, which establishes in a solid after the crystallographic fusion of colloidal precursors was estimated to be R_{Au-Au} = 23 nm for a nanoparticle mixture in Figure 3a and R_{Au-Au} = 34 nm for that displayed in Figure 3b (see the Supporting Information section for details of calculation).

As Figure 3 indicates, a sizable enhancement in the film extinction coefficient is reached by using 0.2–0.5% of Au NPs which corresponds to a R_{Au-Au} range of 23–34 nm. To understand whether this level of Au doping can noticeably shorten the carrier diffusion length in a solid, we have measured the FL lifetime of several mixed films (Figure 5). The FL intensity decay of NC solids has been previously shown to exhibit two distinguishable components, the fast and the slow, corresponding to the exciton dissociation and free carrier recombination processes, respectively (see Figure S4).[48] Such biexponential character of the PbS emission decay can be identified in present measurements of PbS-only matrices, shown by the red curve in Figure 4. Upon addition of Au NPs at a 0.3% volume fraction level, the slow decay component decreases
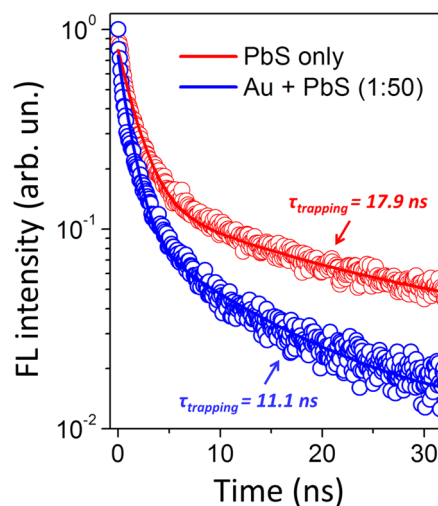

Figure 4. Effect of Au doping on carrier diffusion length in (Au, PbS) nanocrystal solids estimated using the fluorescence lifetime technique. The inclusion of Au NPs into a PbS nanocrystal array leads to the reduction of the slow decay component of the PbS band gap emission, which mirrors the decrease in the carrier diffusion length.[48] Meanwhile, the decline of the fast decay component in (Au, PbS) nanocrystal solids reflects an increase in the rate of exciton dissociation.

from 17.9 to 11.1 ns (blue curve), which implies a reduction in the carrier diffusion length, $l_{diff} \sim (\tau_{slow})^{1/2}$ (assuming that the carrier mobility remains the same).[48] Since the diffusion length is inversely proportional to the film resistance, one can expect a reduction of the current density arising just from the effect of additional scattering in a mixed film. The reduction in the fast component of the FL decay (from 1.68 to 1.13 ns) may imply a greater rate of

exciton dissociation in a mixed film induced by Au scattering. For instance, if the diffusion length of an exciton (not to be confused with the free carrier diffusion length) in the PbS film is greater than R_{Au-Au}, one can expect a noticeable effect of Au doping on the exciton splitting rate, as reflected by the changes in the fast decay component.

To observe an experimental signature of the Au-to-PbS energy transfer, we have performed a set of photoexcitation (PLE) measurements. Within this approach, one can unambiguously distinguish between the contributions of Au and PbS domains into the exciton generation. To this end, the excitation of Au-doped PbS films featuring small-diameter ($d = 2.3$ nm)
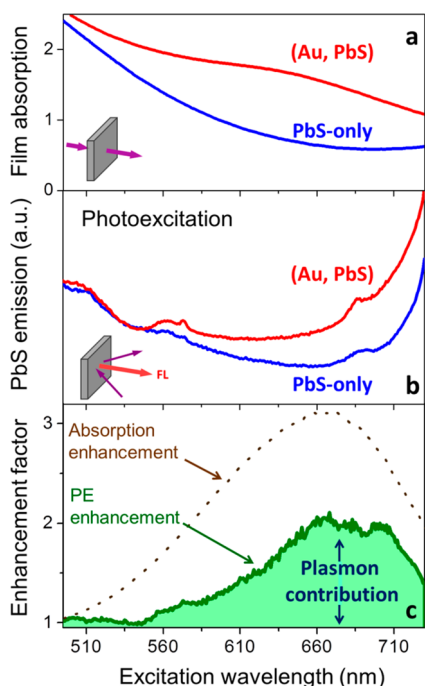

Figure 5. Effect of Au doping on the PbS exciton generation in plasmonic films. (a) The comparison of the optical absorption between (0.3%-Au, PbS) and PbS-only solids ($d_{PbS} \approx 2.3$ nm). (b) The photoexcitation spectrum of a (0.3%-Au, PbS) solid (red curve) is compared to that of PbS-only films. The FL signal was measured at $\lambda = 750$ nm. (c) The fluorescence enhancement factor (red curve) calculated by dividing the normalized photoexcitation spectrum of a mixed matrix (Au, PbS) by that of a PbS-only film. The corresponding absorption enhancement factor obtained by dividing the red by the black curve in (a) is shown for comparison (dotted line).

PbS NCs was performed in the 500−735 nm range, covering both Au and PbS absorption bands, while the emission detector was set at the peak of the PbS band gap fluorescence. According to Figure 5b, the observed photoexcitation profile of the Au-doped films (red curve) exhibits a clear contribution of the plasmon resonance, which is absent in PbS-only devices (black curve). Likewise, the observed PLE feature of Au correlates well with the plasmon shoulder in the film's absorption spectrum (Figure 5a, red curve). This is clearly seen through the comparison of the absorption and photoexcitation enhancement factors, obtained by dividing the corresponding spectra of Au-doped films with their PbS-only "baselines". According to Figure 5c, the maximum of the plasmon contribution into PbS exciton generation falls close to the absorption enhancement maximum (dotted line). On the basis of these results, we can conclude that a sizable portion of PbS excitons arises due to the plasmon absorption of doped films.

Photovoltaic characteristics of plasmonic films were explored using a depleted heterojunction solar cell architecture (Table 1),[49] schematically illustrated in Figure 2a. In this geometry, the $p-n$ junction is formed at the boundary of a (Au, PbS) nanoparticle absorber and a TiO_2 layer, which separates the photoinduced charges between Fluorine-doped tin oxide (FTO) and Au/Pd electrodes. To fabricate a photovoltaic cell from nanoparticle solutions, a matrix-encapsulated (Au, PbS) solid containing 0.3% of Au by volume was deposited on top of a TiO_2 film followed by sputtering of 20−60 nm of Au/Pd electrodes. The development of a TiO_2 film was performed by spin-coating the DyeSol TiO_2 nanoparticle precursor onto FTO-coated glass (resistance = 12 Ω/sq) followed by annealing at 450−480 °C to remove organic traces (see the Methods section). Preparation of the light-absorbing layer involved spin-coating a mixture of Au/CdS and PbS/CdS core/shell NCs, capped with original ligands, onto a TiO_2 layer using 8−10 LbL cylces, totaling 350−400 nm. The film was heated to 150 °C for ~15 min after every three cycles. Upon completion, the pores of the resulting solid were further filled with additional ZnS (typically 4 SILAR cycles), and the film was capped with Au/Pd electrodes through a shadow mask. The area of each metal pixel was 0.03 cm².

TABLE 1. Summary of Photovoltaic Characteristics for Four Types of Investigated Nanocrystal Solar Cells, Including Matrix-Encapsulated PbS, Matrix-Encapsulated (Au, PbS), MPA-Linked PbS, and MPA-Linked (Au, PbS)[a]

cell type	CdS-encapsulated PbS-only	CdS-encapsulated (0.3%-Au, PbS)	MPA-linked PbS-only	MPA-linked (0.3%-Au, PbS)
N	16	9	9	4
V_{OC} (V)	0.522 ± 0.003	0.446 ± 0.002	0.535 ± 0.005	0.298 ± 0.005
J_{SC} (mA/cm^{-2})	20.71 ± 0.50	29.45 ± 0.83	22.05 ± 1.11	3.95 ± 0.41
FF (%)	37.56 ± 0.90	31.84 ± 1.05	34.43 ± 1.10	28.36 ± 1.52
PCE (%)	4.0 ± 0.2	4.2 ± 0.1	4.1 ± 0.2	0.3 ± 0.1

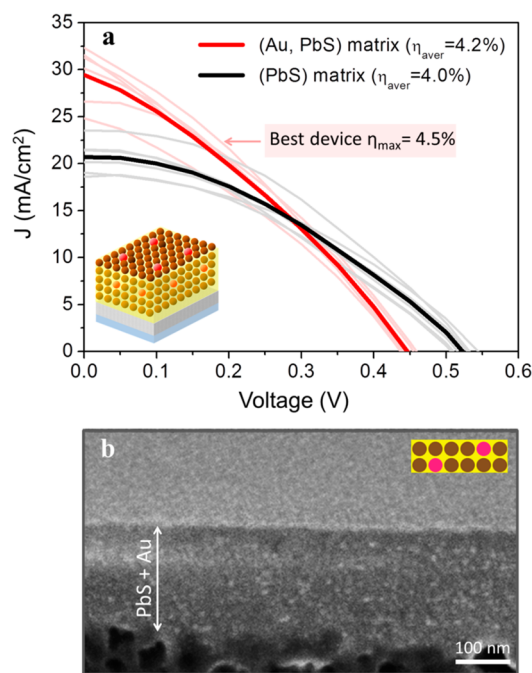[a] The plasmonic devices contained 0.3% of Au by volume.

Figure 6. (a) The comparison of $J-V$ characteristics obtained from a plasmonic (Au, PbS) and a nonplasmonic (PbS-only) nanocrystal solar cells. Both devices were fabricated by sandwiching a CdS-encapsulated nanoparticle layer (∼350−400 nm) between a Au/Pd counter electrode and a 300 nm TiO$_2$ layer, under the requirement that both solids exhibit similar optical densities. On average, Au-doped cells (red curves) showed greater J_{SC} but lower V_{OC} values relative to PV cells containing PbS-only absorber (black curves). The overall performance of Au-doped cells was slightly greater than those of PbS only devices, with the best cell showing PCE of 4.5%. (b) Scanning electron microscope image of a plasmonic (Au, PbS) nanocrystal film in a fabricated solar cell.

Figure 6 compares the photovoltaic performance of plasmonic (Au, PbS) and semiconductor-only nanocrystal solar cells configured to have similar optical densities in the visible range ($\lambda \approx 550$ nm). The overall trend observed for several plasmonic films was an enhanced short circuit current, J_{SC} (gain of 41 ± 3%) as measured relative to PbS-only devices and a somewhat lower value of an open circuit voltage, V_{OC} (drop of 15 ± 0.5%). The latter outcome can be attributed to pinning of the PbS Fermi level at defects forming along the Au/semiconductor interface.

The observed enhancement of the short circuit current in (Au, PbS) devices can be attributed to two possible factors: better carrier extraction from a thinner absorber and an enhanced exciton generation due to near-field Au-to-PbS energy transfer. Since the average J_{SC} of PbS-only devices utilizing a thinner absorber (at 80% optical density of a regular cell) was lower than those tested in Figure 6a, the difference in the absorber thickness alone cannot explain an enhanced current density in plasmonic films. Furthermore, a greater value of J_{SC} was achieved despite the reduced carrier lifetime in Au-doped cells (see Figure 4). This fact strongly suggests an increased carrier density in
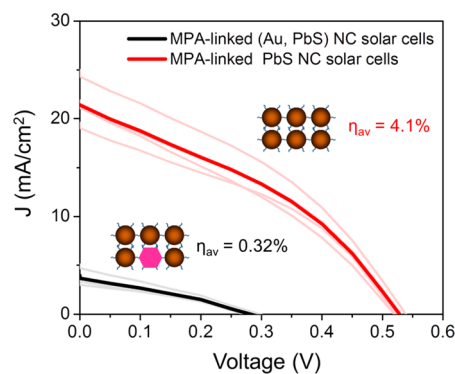
Figure 7. Photovoltaic performance of plasmonic solar cells fabricated by linking PbS and Au nanoparticles with MPA ligands. $J-V$ characteristics of a plasmonic (Au, PbS) device are compared to those of MPA-linked PbS nanocrystal solar cells, fabricated using the depleted heterojunction architecture depicted in Figure 2a. The PCE of Au-doped cells (black curves) is significantly lower than that of PbS-only device (red curves). The low photoconductivity is attributed to enhanced carrier trapping in Au NPs, which shortens the carrier diffusion length.

plasmonic solids, which is sufficient to overcome additional trapping losses resulting from Au scattering. The enhanced J_{SC} in Au-doped devices has contributed to the overall growth in the average efficiency of nanocrystal solar cells from 4.0% (PbS-only) to 4.2% (Au, PbS). The cumulative gain in PCE reflects a combined effect of the enhanced exciton generation in mixed Au+PbS solids and a lower photovoltage resulting from Fermi level pinning.

To stress the importance of Au encapsulation in plasmonic solar cells, we have replaced an insulating shell of CdS on Au surfaces with low-potential barrier 3-mercaptopropionic acid (MPA) ligands. These molecules facilitate the charge transfer between nanoparticles in a solid leading to the best performing nanocrystals devices reported to date.[50,51] In this work, the absorber layer was fabricated through a conventional ligand-linking strategy, *via* processing of OLAM-capped Au NPs and OA-capped PbS NCs into MPA-linked (Au, PbS) solids. The $J-V$ characteristics of these devices comprising 0.3% of Au NPs by volume are shown in Figure 7. The comparison with nonplasmonic cells utilizing MPA-linked PbS NC films reveals a significant performance reduction associated with the addition of Au. Notably, the same level of Au doping in matrix-encapsulated devices has resulted in a 4.2% of PCE, but yielded only 0.32% in the case of MPA-linked cells. The inferior performance of MPA-linked (Au, PbS) films implies an increase in the rate of carrier scattering processes for solids where Au doping produces just a moderate, 30−40% enhancement of the optical density. Such a considerable effect of Au dopants on the carrier diffusion length necessitates the use of an insulating shell on metal surfaces that reduces the semiconductor-to-metal charge transfer rate.

CONCLUSIONS

In conclusion, we have explored the feasibility of utilizing near-field energy transfer as an absorption enhancement strategy in plasmonic nanocrystal solar cells. The use of strongly confined radiation of surface plasmons can increase the optical density of photovoltaic devices beyond the theoretical limit of far-field scattering. In this work, the near-field confinement of light was achieved through the use of small-diameter Au nanoparticles embedded into a PbS nanocrystal solid. The absorber layer was fabricated using a matrix encapsulation scheme, which offers two important benefits: reduced carrier scattering on Au centers and improved stability of heat-prone plasmonic films. The contribution of the near-field emission in Au nanoparticles toward the charge carrier generation was manifested through the observation of an enhanced short circuit current and improved power conversion efficiency of prototype (Au, PbS) solar cells, as measured relative to PbS-only devices. Conceptually, this work demonstrates the possibility of utilizing near-field emission of surface plasmons for improving the performance of photovoltaic devices, which could be harnessed as a novel strategy of solar energy conversion.

METHODS

Materials. Lead(II) oxide powder (PbO, 99.999% Aldrich), 1-octadecene (ODE, 90% Aldrich), oleic acid (OA, 90% Aldrich), bis(trimethylsilyl) sulfide ((TMS)$_2$S, Aldrich, synthetic grade), acetone (anhydrous Amresco, ACS grade), hexane (anhydrous, 95% Aldrich), ethanol (anhydrous, 95% Aldrich), cadmium oxide (CdO, 99.99%, Aldrich), sodium sulfide nonahydrate (Na$_2$S·9H$_2$O, 98% Alfa Aesar), sulfur (S$_8$, 99.999% Acros), methanol (anhydrous, 99.8% Aldrich), isopropanol (anhydrous, 99.8% Acros), toluene (anhydrous, 99.8% Aldrich), tributylphosphine (TBP, 97%, Aldrich), 3-mercaptopropionic acid (MPA, 99%, Alfa Aesar), zinc acetate (98+% Acros), silver nitrate (AgNO$_3$ 99%, Aldrich), gold(III) chloride (AuCl$_3$ 99%, Acros Organics), titanium dioxide (DSL 90T, DyeSol), terpineol (MP Biochemicals), titanium chloride (TiCl$_4$, 99.99% Aldrich) and cadmium nitrate tetrahydrate (Cd(NO$_3$)$_2$·4H$_2$O, 99.999%, Aldrich) were used as received without any further purification. Oleylamine (tech., 70%, Aldrich) was pumped for 1 h at 120 °C and then stored under argon atmosphere prior using. Fluorine-doped tin oxide (FTO, SnO$_2$/F) glass (TEC 15, 12—14 Ohm/sq) was obtained from Pilkington Glass. All reactions were performed under argon atmosphere using the standard Schlenk technique. The centrifuge used for precipitation operated at 7200 rpm.

Synthesis of PbS Nanocrystals. PbS NCs were synthesized according to the procedure reported by Hines et al.[52] A mixture of 0.49 g of PbO, 18 mL of ODE, and 1.5 mL of OA was degassed in a 3-neck flask at 120 °C for 2 h, switched to argon flow, and kept at 135 °C until injection. At the same time, 10 mL of ODE was degassed at 120 °C for 2 h in one-neck flask, switched to argon flow, and kept at room temperature. Later, 0.21 mL of (TMS)$_2$S was added to ODE at room temperature under argon flow. The resulting (TMS)$_2$S/ODE mixture was injected into the Pb precursor solution at 135 °C, while stirring. The reaction was stopped after 2 min by removing the flask from the heating mantle and placing it into a cold water bath. Fabricated PbS nanocrystals were isolated from the mixture by precipitating with acetone, centrifuging, and redispersing in hexane. The cleaning procedure has been repeated 2 times, after which nanocrystals were finally redispersed in hexane (~8 mL). The prepared NCs had 1S peak at 1020 nm.

Synthesis of PbS/CdS Core/Shell NCs through Cation Exchange. The NCs were synthesized according to the procedure reported by Pietryga et al.[53] A mixture of 0.2 g of CdO, 1.5 mL of OA, and 6 mL of ODE was heated to 235 °C under argon until the solution became clear. The reaction mixture was kept at 55 °C under argon flow. Then, 4 mL of PbS was injected to the Cd^{2+} precursor and the reaction was immediately quenched by removing the flask from a heating mantle and placing into a cold water bath. The PbS/CdS NCs were isolated by centrifuging with ethanol. The precipitate obtained during centrifuge was dissolved in 2—3 mL of hexane. The cleaning procedure has been repeated 2 times, after which nanocrystals were finally redispersed in hexane (~4 mL). The blue shift was observed in the prepared core/shell NCs with the value of $\Delta\lambda = 50-60$ nm (shell thickness ≈0.25 nm).

Synthesis of Oleylamine-Capped Au Nanocrystals (NCs). Au NCs were synthesized according to previously reported methodology.[54] In a typical synthesis, 0.011 g of AuCl$_3$ and 5 mL of oleylamine were loaded in a one-neck flask and allowed to react at 100 °C for 30 min under argon atmosphere. During this time, the reaction mixture's color changed from transparent yellow to orange (indicating the formation of Au-oleate complexes), and then finally to purple (indicating the formation of oleylamine-capped Au NPs). The reaction was stopped by removing the flask from the heating mantle and allowed to cool to room temperature. Then, the solution was transferred from the flask into centrifuge tubes and precipitated with ethanol. After the centrifugation, the supernatant was discarded and the pellet was dissolved in chloroform. The cleaning cycle was repeated one more time and the final product was redispersed and stored in 5 mL of chloroform. The final product contained Au NPs with an average diameter of 5 nm and a surface plasmon resonance (LSPR) peak at $\lambda \approx 525$ nm.

Synthesis of Oleylamine-Capped Au/Ag Core/Shell NCs. The growth of Ag shell was performed according to the procedure adopted by Shore et al.[55] Approximately a quarter of Au NPs from the previous step were mixed with 5 mL of oleylamine. The mixture was heated to 120 °C while stirring. At this point, 1.05×10^{-2} M aqueous solution of Ag$^+$, prepared by sonication 0.089 g of AgNO$_3$ in 5 mL of deionized water, was injected stepwise into the Au-seed reaction flask (0.2 mL every 10 min). The average thickness of the Ag shell surrounding the Au NPs was tracked by the position of the localized surface plasmon resonance (LSPR) peak. After every 10 min of the shell growth period, a sample was taken from the reaction flask for steady-state spectroscopic analysis. The LSPR peak of NPs comprised strictly of Au was centered about $\lambda_{Au} \approx 525$ nm, and this peak blue-shifted closer to the position of pure Ag NP's LSPR peak ($\lambda_{Ag} \approx 415$ nm for Ag NPs of similar dimensions) as the Ag shell grew in thickness. After observing the desired LSPR peak at 455 nm ($\Delta\lambda = 70$ nm), the reaction mixture was cooled down to the room temperature by removing the flask from a heating mantle. The synthesized Au/Ag nanocrystals were isolated from the mixture by precipitating with ethanol, centrifuging, and redispersing in chloroform.

Synthesis of Au/Ag$_2$S NCs from Au/Ag. The Au/Ag$_2$S NCs were synthesized according to the procedure adapted from Zhang et al.[56] Briefly, a solution of sulfur precursor, which was prepared by sonication of 0.005 g of S$_8$ powder in 2 mL of oleylamine, was injected into a 25 mL two-neck flask containing the entire amount of Au/Ag solution fabricated in the previous step. The sulfur precursor was added in 0.2 mL increments to the solution of Au/Ag core/shell NCs, which were under argon and being vigorously stirred, and then left to react for 10 min. After 10 min, a sample was taken for spectral analysis. Sulfur was added in this way until the LSPR absorption peak had red-shifted to ~630 nm. The NCs were then cleaned once by adding 10 mL of ethanol to the reaction solution and centrifugating the solution. Under argon, the precipitated NCs were then suspended in 4 mL of toluene.

Synthesis of Au/CdS NCS from Au/Ag₂S. Au/CdS NCs were fabricated using a procedure inspired by Zhang *et al.*[56] To this end, a toluene solution of Au/Ag₂S NCs from the previous step was combined with 1 mL of oleylamine, placed in a two-neck flask and heated up to 60 °C under argon atmosphere. The cadmium precursor, which was prepared in a glass vial by sonication of 0.12 g (0.39 mmol) of Cd(NO₃)₂·4H₂O in 1 mL of methanol, was quickly injected into a reaction flask and solution was allowed to stir at elevated temperature for 10 min. To initiate the cation exchange reaction, 0.1 mL of TBP was added to the mixture and solution was left for 2 h at 60 °C under vigorous stirring. The growth of the shell was accompanied by the blue-shift of the LPSR peak. To isolate final product, 10 mL of methanol was added to the reaction mixture, which was subsequently centrifuged. The precipitate was then dissolved and stored in hexane.

Preparation of the Glass Substrate. FTO-coated glass was cut into 2.5 cm × 2.5 cm squares, then washed by hand with detergent (Alconox), and rinsed clean in deionized water. It was then sonicated in methanol, acetone, and isopropyl alcohol for 5 min in each solvent.

Fabrication of Nanocrystal Solids. The fabrication of all-inorganic NC films (SMENA) was performed using a previously reported methodology.[45,57] For each layer, the solution of PbS/CdS NCs in hexane (concentration 20 mg/mL) or a mixture of PbS/CdS and Au/CdS NCs was deposited on the glass substrate and span at 3000 rpm for 10 s. Subsequently, 7–10 drops of MPA/Methanol solution (ratio 1:3) were deposited on the center of the glass slide, soaked for 10 s and spun at 3000 rpm for 10 s. After the MPA treatment, the film was washed by covering with 10 drops of methanol and spinning the slide for 10 s, followed by rinsing with hexane in the same manner. Upon the deposition of 2 layers, the films were annealed at 140–150 °C for 15 min. The total amount of layers was varied from 3 to 4. Ratios of PbS/CdS to Au/CdS were calculated using a volume fraction of each material in the mixture (see Supporting Information).

Fabrication of Solar Cells. *Preparation of TiO₂ Electrodes.* The deposition of the TiO₂ layer was performed using a previously reported approach.[45,58] To this end, dry and clean SnO₂/F-coated glass substrates were immersed in a 75 mM solution of TiCl₄ in deionized water and allowed to soak at 70 °C for 30 min. The substrate was then rinsed with deionized water, dried under argon, heated to 450 °C for 1 h, and then allowed to cool to room temperature. Meanwhile, the mixture of TiO₂ DyeSol paste and terpineol (1:3 ratio by weight) was sonicated until solution became homogeneous. Three drops of the freshly prepared TiO₂ solution was placed in the center of a dry TiCl₄-treated SnO₂/F-coated glass slide and spun for 6 s at 700 rpm and for 1 min at 2900 rpm. The substrate was then annealed outside the glovebox (ambient oxygen environment) at 450–500 °C to remove organic matter.

Deposition of Mixed (Au, PbS) Nanoparticle Films from Solution. For the SMENA solar cells fabrication the nanocrystals were deposited using an aforementioned approach (see Fabrication of Nanocrystal Solids). The total 8–10 layers were deposited on the TiO₂ electrode.

MPA-linked NC films were deposited using a layer-by-layer spin-coating process under argon atmosphere. Each layer of nanocrystals was deposited by placing 3–5 drops of the mixture on the spinning substrate (3000 rpm) with subsequent treatment with MPA solution (*i.e.*, MPA:methanol = 3:1) and rinsing the film with methanol and hexane. The total of 6–8 layers of the NCs were deposited. Ratios of PbS to Au were calculated using a volume fraction of each material in the mixture (see Supporting Information).

In-Filling of SMENA Pores with ZnS. For the pore-filling process, the successive ionic layer adsorption and reaction (SILAR) method was applied.[59] Briefly, the deposition of additional layers of ZnS was conducted by sequential soaking of the annealed NC films in methanol solutions of Zn and S precursors. For this purpose, the zinc bath was prepared by dissolution of 0.10 g of zinc acetate in 20 mL of methanol and the sulfur bath by placing 0.098 g of Na₂S·9H₂O in 20 mL of methanol. One SILAR cycle included soaking of the film in the zinc bath for 10 min, then rinsing the film with *fresh* methanol for 5 min, then

soaking it in the sulfur bath for 1 min with sequential washing in methanol. 2–4 cycles of pores filling process was applied for all-inorganic films followed by annealing at 150 °C for 15 min.

Deposition of Au/Pd Counter Electrodes. To complete the cell assembly, 60–90 nm of gold–palladium (Au–Pd, 40/60) counter electrodes were coated on top of the film using Polaron E500 sputter, which was equipped with a ≈2 mm diameter shadow mask generating 16 pixels in each device. The area of each pixel was estimated to be 0.03 cm².

Characterization. Absorbance spectra were recorded using a CARY 50 scan and Shimadzu UV-3600 UV–vis–NIR spectrophotometers. Photoluminescence measurements were performed using Jobin Yvon Fluorolog FL3–11 fluorescence spectrophotometer. High resolution transmission electron microscopy (TEM) measurements were carried out using JEOL 311UHR operated at 300 kV. Specimens were prepared by depositing a drop of NP solution in organic solvent onto a carbon-coated copper grid and allowing it to dry in air. I–V data was measured using a Keithley 2400 source-meter under ambient conditions. Characteristics were performed under AM 1.5 G (100 mW/cm²) solar simulator on the I–V data acquisition system from PV Measurements, Inc. X-ray powder diffraction (XRD) measurements were carried out on a Scintag XDS-2000 X-ray powder diffractometer. FL lifetime measurements in 900 nm region were performed using a time-correlated single photon counting setup utilizing SPC-630 single-photon counting PCI card (Becker & Hickle GmbH), picosecond diode laser operating at 400 nm, as an excitation source (Picoquant), an id50 avalanche photodiode (Quantique), and long-pass optical filters with edges at 400, 532, and 750 nm.

Photoexcitation. Steady-state photoexcitation spectra were measured using a PTI QuantaMaster spectrofluorometer with a xenon lamp light source. Excitation scan was performed in the range 510–735 nm with the detection on PbS band gap emission at 750 nm. The spectra were collected at 45° for the solid films and integrated for 10 s per nanometers for better noise to signal ratio.

Conflict of Interest: The authors declare no competing financial interest.

Supporting Information Available: Experimental details, additional TEM and HRTEM images. This material is available free of charge *via* the Internet at http://pubs.acs.org.

REFERENCES AND NOTES

1. Rycenga, M.; Cobley, C. M.; Zeng, J.; Li, W.; Moran, C. H.; Zhang, Q.; Qin, D.; Xia, Y. Controlling the Synthesis and Assembly of Silver Nanostructures for Plasmonic Applications. *Chem. Rev.* **2011**, *111*, 3669–3712.

2. Jiang, R.; Li, B.; Fang, C.; Wang, J. Metal/Semiconductor Hybrid Nanostructures for Plasmon-Enhanced Applications. *Adv. Mater.* **2014**, *26*, 5274–5309.

3. Yu, W. W.; Qu, L.; Guo, W.; Peng, X. Experimental Determination of the Extinction Coefficient of CdTe, CdSe, and CdS Nanocrystals. *Chem. Mater.* **2003**, *15*, 2854–2860.

4. Navarro, J. R. G.; Werts, M. H. V. Resonant Light Scattering Spectroscopy of Gold, Silver and Gold-Silver Alloy Nanoparticles and Optical Detection in Microfluidic Channels. *Analyst* **2013**, *138*, 583–592.

5. Cademartiri, L.; Montanari, E.; Calestani, G.; Migliori, A.; Guagliardi, A.; Ozin, G. A. Size-Dependent Extinction Coefficients of PbS Quantum Dots. *J. Am. Chem. Soc.* **2006**, *128*, 10337–10346.

6. Shrotriya, V.; Ouyang, J.; Tseng, R. J.; Li, G.; Yang, Y. Absorption Spectra Modification in Poly(3-hexylthiophene):methanofullerene Blend Thin Films. *Chem. Phys. Lett.* **2005**, *411*, 138–143.

7. Liu, X.; Atwater, M.; Wang, J.; Huo, Q. Extinction Coefficient of Gold Nanoparticles with Different Sizes and Different Capping Ligands. *Colloids Surf., B* **2007**, *58*, 3–7.

8. Peng, Q.; Wyman, I. W.; Han, D.; Liu, G. Influence of Molecular Weight on the Spectroscopic Properties of a Series of Well-Defined Poly(3-hexylthiophene) Polymers. *Can. J. Chem.* **2011**, *89*, 27–33.

9. Boriskina, S. V.; Ghasemi, H.; Chen, G. Plasmonic Materials for Energy: from Physics to Applications. *Mater. Today* **2013**, *16*, 375.

10. Park, Y. S.; Ghosh, Y.; Xu, P.; Mack, N. H.; Wang, H. L.; Hollingsworth, J. A.; Htoon, H. Single-Nanocrystal Photoluminescence Spectroscopy Studies of Plasmon−Multiexciton Interactions at Low Temperature. *J. Phys. Chem. Lett.* **2013**, *4*, 1465–1470.

11. LeBlanc, S. J.; McClanahan, M. R.; Jones, M.; Moyer, P. J. Enhancement of Multiphoton Emission from Single CdSe Quantum Dots Coupled to Gold Films. *Nano Lett.* **2013**, *13*, 1662–1669.

12. Aydin, K.; Ferry, V. E.; Briggs, R. M.; Atwater, H. A. Broadband Polarization-Independent Resonant Light Absorption Using Ultrathin Plasmonic Super Absorbers. *Nat. Commun.* **2011**, *2*, 517.

13. Green, M. A.; Pillai, S. Harnessing Plasmonics for Solar Cells. *Nat. Photonics* **2012**, *6*, 130–132.

14. Atwater, H. A.; Polman, A. Plasmonics for Improved Photovoltaic Devices. *Nat. Mater.* **2010**, *9*, 205–213.

15. Mubeen, S.; Hernandez-Sosa, G.; Moses, D.; Lee, J.; Moskovits, M. Plasmonic Photosensitization of a Wide Band Gap Semiconductor: Converting Plasmons to Charge Carriers. *Nano Lett.* **2011**, *11*, 5548–5552.

16. Sobhani, A.; Knight, M. W.; Wang, Y.; Zheng, B.; King, N. S.; Brown, L. V.; Fang, Z.; Nordlander, P.; Halas, N. J. Narrow Band Photodetection in the Near-Infrared with a Plasmon-Induced Hot Electron Device. *Nat. Commun.* **2013**, *4*, 1643.

17. Knight, M. W.; Sobhani, H.; Nordlander, P.; Halas, N. J. Photodetection with Active Optical Antennas. *Science* **2011**, *332*, 702–704.

18. Mubeen, S.; Lee, J.; Singh, N.; Krämer, S.; Stucky, G. D.; Moskovits, M. An Autonomous Photosynthetic Device in which All Charge Carriers Derive from Surface Plasmons. *Nat. Nanotechnol.* **2013**, *8*, 247–251.

19. Paz-Soldan, D.; Lee, A.; Thon, S. M.; Adachi, M. M.; Dong, H.; Maraghechi, P.; Yuan, M.; Labelle, A. J.; Hoogland, S.; Liu, K.; et al. Jointly Tuned Plasmonic−Excitonic Photovoltaics Using Nanoshells. *Nano Lett.* **2013**, *13*, 1502–1508.

20. Gan, Q.; Bartoli, F. J.; Kafafi, Z. H. Plasmonic-Enhanced Organic Photovoltaics: Breaking the 10% Efficiency Barrier. *Adv. Mater.* **2013**, *25*, 2385–2396.

21. Tian, Z. B.; Wang, L. Q.; Jia, L. S.; Li, Q. B.; Song, Q. Q.; Su, S.; Yang, H. A Novel Biomass Coated Ag-TiO$_2$ Composite as a Photoanode for Enhanced Photocurrent in Dye-Sensitized Solar Cells. *RSC Adv.* **2013**, *3*, 6369–6376.

22. Niezgoda, J. S.; Yap, E.; Keene, J. D.; McBride, J. R.; Rosenthal, S. J. Plasmonic Cu$_x$In$_y$S$_2$ Quantum Dots Make Better Photovoltaics Than Their Nonplasmonic Counterparts. *Nano Lett.* **2014**, *14*, 3262–3269.

23. Rand, B. P.; Peumans, P.; Forrest, S. R. Long-Range Absorption Enhancement in Organic Tandem Thin-Film Solar Cells Containing Silver Nanoclusters. *J. Appl. Phys.* **2004**, *96*, 7519–7526.

24. Fang, C.; Jia, H.; Chang, S.; Ruan, Q.; Wang, P.; Chen, T.; Wang, J. (Gold Core)/(Titania Shell) Nanostructures for Plasmon-Enhanced Photon Harvesting and Generation of Reactive Oxygen Species. *Energy Environ. Sci.* **2014**, *7*, 3431–3438.

25. Zhang, Y.; Ouyang, Z.; Stokes, N.; Jia, B.; Shi, Z.; Gu, M. Low Cost and High Performance Al Nanoparticles for Broadband Light Trapping in Si Wafer Solar Cells. *Appl. Phys. Lett.* **2012**, *100*, 151101.

26. Zhang, Y.; Chen, X.; Ouyang, Z.; Lu, H.; Jia, B.; Shi, Z.; Gu, M. Improved Multicrystalline Si Solar Cells by Light Trapping from Al Nanoparticle Enhanced Antireflection Coating. *Opt. Mater. Express* **2013**, *3*, 489–495.

27. Tan, J. Z. Y.; Fernandez, Y.; Liu, D.; Maroto-Valer, M.; Bian, J.; Zhang, X. Photoreduction of CO$_2$ using Copper-Decorated TiO$_2$ Nanorod Films with Localized Surface Plasmon Behavior. *Chem. Phys. Lett.* **2012**, *531*, 149–154.

28. Jia, B.; Chen, X.; Saha, J. K.; Qiao, Q.; Wang, Y.; Shi, Z.; Gu, M. Concept to Devices: from Plasmonic Light Trapping to Upscaled Plasmonic Solar Modules. *Photon. Res.* **2013**, *1*, 22–27.

29. Chen, X.; Jia, B.; Saha, J. K.; Cai, B.; Stokes, N.; Qiao, Q.; Wang, Y.; Shi, Z.; Gu, M. Broadband Enhancement in Thin-Film Amorphous Silicon Solar Cells Enabled by Nucleated Silver Nanoparticles. *Nano Lett.* **2012**, *12*, 2187–2192.

30. Wang, C.; Choy, W.; Duan, C.; Fung, D.; Sha, W.; Xie, F.; Huang, F.; Cao, Y. Optical and Electrical Effects of Gold Nanoparticles in the Active Layer of Polymer Solar Cells. *J. Mater. Chem.* **2012**, *22*, 1206–1211.

31. Yablonovitch, E. Statistical Ray Optics. *J. Opt. Soc. Am.* **1982**, *72*, 899–907.

32. Yu, Z.; Raman, A.; Fan, S. Fundamental Limit of Nanophotonic Light Trapping in Solar Cells. *Proc. Natl. Acad. Sci. U. S. A.* **2010**, *107*, 17491–17496.

33. Munday, J. N.; Callahan, D. M.; Atwater, H. A. Light Trapping beyond $4n^2$ Limit in Thin Waveguides. *Appl. Phys. Lett.* **2012**, *100*, 121121.

34. Schiff, E. A. Thermodynamic Limit to Photonic-Plasmonic Light-Trapping in Thin Films on Metals. *J. Appl. Phys.* **2011**, *110*, 104501.

35. Aruda, K. O.; Tagliazucchi, M.; Sweeney, C. M.; Hannah, D. C.; Weiss, E. A. The Role of Interfacial Charge Transfer-Type Interactions in the Decay of Plasmon Excitations in Metal Nanoparticles. *Phys. Chem. Chem. Phys.* **2013**, *15*, 7441–7449.

36. Link, S.; Burda, C.; Mohamed, M. B.; Nikoobakht, B.; El-Sayed, M. A. Femtosecond Transient-Absorption Dynamics of Colloidal Gold Nanorods: Shape Independence of the Electron-Phonon Relaxation Time. *Phys. Rev.* **2000**, *61*, 6086–6090.

37. Chen, G. *Nanoscale Energy Transfer and Conversion*; Oxford University Press: New York, 2005.

38. Ramakrishna, G.; Dai, Q.; Zou, J.; Huo, Q.; Goodson, T., III. Interparticle Electromagnetic Coupling in Assembled Gold-Necklace Nanoparticles. *J. Am. Chem. Soc.* **2007**, *129*, 1848.

39. Mukherjee, S.; Libisch, F.; Large, N.; Neumann, O.; Brown, L. V.; Cheng, J.; Lassiter, J. B.; Carter, E. A.; Nordlander, P.; Halas, N. J. Hot Electrons Do the Impossible: Plasmon-Induced Dissociation of H$_2$ on Au. *Nano Lett.* **2013**, *13*, 240–247.

40. Hung, W. H.; Aykol, M.; Valley, D.; Hou, W.; Cronin, S. B. Plasmon Resonant Enhancement of Carbon Monoxide Catalysis. *Nano Lett.* **2010**, *10*, 1314–1318.

41. Linic, S.; Christopher, P.; Ingram, D. B. Plasmonic-Metal Nanostructures for Efficient Conversion of Solar to Chemical Energy. *Nat. Mater.* **2011**, *10*, 911–921.

42. Sun, M.; Xu, H. A Novel Application of Plasmonics: Plasmon-Driven Surface-Catalyzed Reactions. *Small* **2012**, *8*, 2777–2786.

43. Joulain, K.; Muletb, J. P.; Marquierb, F.; Carminatib, R.; Greffet, J. J. Surface Electromagnetic Waves Thermally Excited: Radiative Heat Transfer, Coherence Properties and Casimir Forces Revisited in the Near Field. *Surf. Sci. Rep.* **2005**, *57*, 59–112.

44. Choi, H.; Lee, J. P.; Ko, S. J.; Jung, J. W.; Park, H.; Yoo, S.; Park, O.; Jeong, J. R.; Park, S.; Kim, J. Y. Multipositional Silica-Coated Silver Nanoparticles for High Performance Polymer Solar Cell. *Nano Lett.* **2013**, *13*, 2204–2208.

45. Kinder, E.; Moroz, P.; Diederich, G.; Johnson, A.; Kirsanova, M.; Nemchinov, A.; O'Connor, T.; Roth, D.; Zamkov, M. Fabrication of All-Inorganic Nanocrystal Solids through Matrix Encapsulation of Nanocrystal Arrays. *J. Am. Chem. Soc.* **2011**, *133*, 20488–20499.

46. Khon, E.; Lambright, S.; Khon, D.; Smith, B.; O'Connor, T.; Moroz, P.; Imboden, M.; Diederich, G.; Perez-Bolivar, D.; Anzenbacher, P.; et al. Inorganic Solids of CdSe Nanocrystals Exhibiting High Emission Quantum Yield. *Adv. Funct. Mater.* **2012**, *22*, 3714–3722.

47. Moroz, P.; Liyanage, G.; Kholmicheva, N.; Yakunin, S.; Uprety, P.; Bastola, E.; Rijal, U.; Mellott, B.; Subedi, K.; Sun, L.; et al. Infrared Emitting PbS Nanocrystal Solids through Matrix Encapsulation. *Chem. Mater.* **2014**, *26*, 4256–4264.

48. Moroz, P.; Kholmicheva, N.; Mellott, B.; Liyanage, G.; Rijal, U.; Bastola, E.; Huband, K.; Khon, E.; McBride, K.; Zamkov, M. Suppressed Carrier Scattering in CdS-Encapsulated PbS Nanocrystal Films. *ACS Nano* **2013**, *7*, 6964–6977.

49. Pattantyus-Abraham, A. G.; Kramer, I. J.; Barkhouse, A. R.; Wang, X.; Konstantatos, G.; Debnath, R.; Levina, L.; Raabe, I.; Nazeeruddin, M. K.; Gratzel, M.; *et al.* Depleted-Heterojunction Colloidal Quantum Dot Solar Cells. *ACS Nano* **2010**, *4*, 3374–3380.

50. Ip, A. H.; Thon, S. M.; Hoogland, S.; Voznyy, O.; Zhitomirsky, D.; Debnath, R.; Levina, L.; Rollny, L. R.; Carey, G. H.; Fischer, A.; *et al.* Hybrid Passivated Colloidal Quantum Dot Solids. *Nat. Nanotechnol.* **2012**, *7*, 577–582.

51. Chuang, C. H. M.; Brown, P. R.; Bulovic, V.; Bawendi, M. G. Improved Performance and Stability in Quantum Dot Solar Cells through Band Alignment Engineering. *Nat. Mater.* **2014**, *13*, 796–801.

52. Hines, M. A.; Scholes, G. D. Colloidal PbS Nanocrystals with Size-Tunable Near-Infrared Emission: Observation of Post-Synthesis Self-Narrowing of the Particle Size Distribution. *Adv. Mater.* **2003**, *15*, 1844–1849.

53. Pietryga, J. M.; Werder, D. J.; Williams, D. J.; Casson, J. L.; Schaller, R. D.; Klimov, V. I.; Hollingsworth, J. A. Utilizing the Lability of Lead Selenide to Produce Heterostructured Nanocrystals with Bright, Stable Infrared Emission. *J. Am. Chem. Soc.* **2008**, *130*, 4879–4885.

54. Lambright, S.; Butaeva, E. V.; Razgoniaeva, N.; Hopkins, T.; Smith, B.; Perera, D. N.; Corbin, J.; Khon, E.; Thomas, R.; Moroz, P.; *et al.* Enhanced Lifetime of Excitons in Non-Epitaxial Au/CdS Core/Shell Nanocrystals. *ACS Nano* **2014**, *8*, 352–361.

55. Shore, M. S.; Wang, J.; Johnston-Peck, A. C.; Oldenburg, A. L.; Tracy, J. B. Synthesis of Au(Core)/Ag(Shell) Nanoparticles and Their Conversion to AuAg Alloy Nanoparticles. *Small* **2011**, *7*, 230–234.

56. Zhang, J.; Tang, Y.; Lee, K.; Ouyang, M. Nonepitaxial Growth of Hybrid Core-Shell Nanostructures with Large Lattice Mismatches. *Science* **2010**, *327*, 1634–1638.

57. Moroz, P.; Liyanage, G.; Kholmicheva, N.; Yakunin, S.; Uprety, P.; Bastola, E.; Rijal, U.; Mellott, B.; Subedi, K.; Sun, L.; Kovalenko, M. V.; Zamkov, M. Infrared Emitting PbS Nanocrystal Solids through Matrix Encapsulation. *Chem. Mater.* **2014**, *26*, 4256–4264.

58. Kramer, I. J.; Levina, L.; Debnath, R.; Zhitomirsky, D.; Sargent, E. H. Solar Cells Using Quantum Funnels. *Nano Lett.* **2011**, *11*, 3701–3706.

59. Pathan, H. M.; Lokhande, C. D. Deposition of Metal Chalcogenide Thin Films by Successive Ionic Layer Adsorption and Reaction (SILAR) Method. *Bull. Mater. Sci.* **2004**, *27*, 85–111.